RSC Advances

ROYAL SOCIETY OF CHEMISTRY

PAPER

View Article Online
View Journal | View Issue

Check for updates

Cite this: *RSC Adv.*, 2023, **13**, 26122

On the high-temperature phase transition of a new chlorocadmate(II) complex incorporating symmetrical Cd_2Cl_6 clusters: structural, optical and electrical properties†

Hanen Elgahami,*[a] Abderrazek Oueslati,[a] Samia Nasr,[b]
Ferdinando Costantino[c] and Houcine Naïli*[d]

Received 27th June 2023
Accepted 22nd August 2023

DOI: 10.1039/d3ra04289h

rsc.li/rsc-advances

In the present investigation, a new hybrid crystal, with the formula $[(C_4H_9)_4P]_2Cd_2Cl_6$ has been synthesized by the slow evaporation method at room temperature. It was characterized by X-ray diffraction (XRD), Hirshfeld surface, differential scanning calorimetry (DSC), optical measurement and complex impedance. Single crystal X-ray diffraction structural analysis revealed that the title compound crystallizes in the triclinic system with space group $P\bar{1}$ and cell parameters: $a = 11.972$ (1) Å, $b = 15.418$ (1) Å, $c = 15.426$ (2) Å, $\alpha a = 68.71$ (2) °, $\beta = 73.20$ (3) ° and $\gamma = 74.39$ (2)°. The Hirshfeld surface analysis was conducted to investigate intermolecular interactions and associated 2D fingerprint plots, revealing quantitatively the relative contribution of these interactions in the crystal cohesion. DSC studies indicated one phase transition at about 348 K. Optical absorption spectra show that the band gap of $[(C_4H_9)_4P]_2Cd_2Cl_6$ is approximately 2.65 eV. The Nyquist plot showed only one semicircular arc, representing the grain effect in the electrical conduction. The thermal evolution of the conductivity of the grains presents an Arrhenius type behavior, demonstrating that charge carriers have to overcome different energy barriers while conducting and relaxing. Besides, the AC conductivity was analyzed by Jonscher's law and the conduction mechanism is well ensured by the correlated barrier hopping (CBH) model.

1. Introduction

Organic/inorganic hybrid crystals have great importance due to their fascinating structural diversities[1] and potential applications in field-effect transistors,[2,3] electroluminescent devices,[4] photovoltaic cells,[5] light-emitting diodes,[6] Photodetectors,[7] catalysis and so forth.[8] Among such materials, organic/inorganic hybrids of perovskite-type (OIHP) with the general formula $A_xB_yX_z$, where A is an organic cation, B is a metal and X is a halide have been widely investigated for their promising application in solar energy conversion.[9] This is mainly attributed to their excellent properties such as tunable band gaps,[10] high charge carrier mobility,[11] defect tolerance[12] and low-temperature solution processability.[13] In recent years, single perovskite hybrids, especially $CH_3NH_3PbI_3$ ($MAPbI_3$), generated significant interest in electronic and photonic applications due to their special properties. Additionally, fabrication of this hybrid requires relatively low production costs compared to inorganic oxide perovskites.[14] The main advantage of OIHP is the flexibility of their structures. Unlike the parent oxide perovskites with 3D structure, which are relatively rigid, OIHP from the halide family can form structural units of different architectures: isolated 0D, 1D chain, 2D layered and 3D elements. Another class of hybrid materials are called double perovskites with a chemical formula $A_2B_2X_6$ (A = Cs or organic cations; X = Cl, Br, or I), which can be regarded as derivatives of single perovskite $APbX_3$ but with Pb replaced by other metal cations.[15–23] Nevertheless, most double perovskites which are predicted to have good electronic properties, often suffer from instability issues such as phase separation or redox decomposition, *e.g.*, $Cs_2InBiCl_6$ and $Cs_2InSbCl_6$ (ref. 24) while double perovskites that can be synthesized usually show large indirect band gaps.[25–28] Despite this, extensive research efforts are being made to search for novel double perovskites with desired electronic properties and high stability. In this context, the materials based on substituted complex ammoniums with halogenated metals such as Hg, Cd, Zn, Cu *etc.* exhibited highly interesting physical properties.[29–33] For

---

[a] *Laboratory of Spectroscopic Characterization and Optical Materials, Faculty of Sciences, University of Sfax, B.P. 1171, Sfax 3000, Tunisia. E-mail: hanengahami1993@gmail.com*

[b] *Chemistry Department, Faculty of Science, King Khalid University, P.O. Box 9004, Abha 61413, Saudi Arabia*

[c] *Department of Chemistry Biology and Biotechnologies, University of Perugia, Via Elce di Sotto 8, Perugia 06123, Italy*

[d] *Laboratory Physico Chemistry of the Solid State, Department of Chemistry, Faculty of Sciences, University of Sfax, BP 1171, Sfax 3000, Tunisia. E-mail: houcine.naili@fss.rnu.tn*

† Electronic supplementary information (ESI) available. CCDC 2247975. For ESI and crystallographic data in CIF or other electronic format see DOI: https://doi.org/10.1039/d3ra04289h

instance, the Cd(II) ion was chosen due to its adoption of a variety of coordination numbers and geometries[34–37] depending on the crystal packing and ligands where the anionic sub-lattice of the crystal may consist of one- dimensional chain, or a two- to three-dimensional anionic framework.[38,39] Therefore, the coordination chemistry of Cd(II) ions with such ligands is of interest. A very good example is the zero-dimensional (0D) compound of $(Ph_4P)_2Cd_2Br_6$ (ref. 40). Following this route, we synthesized a new organic–inorganic $[(C_4H_9)_4P]_2Cd_2Cl_6$ hybrid by slow evaporation method. The obtained phase was characterized by XRD, Hirshfeld surface analysis, thermal analysis using differential scanning calorimetry (DSC), optical properties by UV-visible spectroscopy and electrical properties are determined with Complex Impedance Spectroscopy.

2. Experimental section

2.1. Synthesis of $[(C_4H_9)_4P]_2Cd_2Cl_6$

The crystals of $[(C_4H_9)_4P]_2Cd_2Cl_6$ compound were synthesized starting from $[(C_4H_9)_4P]Cl$ and $CdCl_2$ precursors which were weighed in the stoichiometric proportion 2 : 2 and were dissolved in aqueous solution, under constant stirring, forming a colorless solution, according to the below equation. The mixture has been slowly evaporated at ambient temperature. After a few days, colorless crystals of $[(C_4H_9)_4P]_2Cd_2Cl_6$, appeared at the bottom of the Petri dish.

Table 1 Crystal data and structure refinement for $[(C_4H_9)_4P]_2Cd_2Cl_6$ crystal

Crystal data	
Chemical formula	$C_{32}H_{72}P_2Cd_2Cl_6$
Molecular weight (g mol−^{1})	956.36
Crystal system	Triclinic
Space group	$P\bar{1}$
Temperature (K)	296
a, b, c (Å)	11.972(1), 15.418(1), 15.426(2)
α, β, γ (°)	68.71(2), 73.20 (3), 74.39(2)
V (Å^3)	2496.4
Z	2
Radiation type	Mo K_α
μ (mm^{-1})	1.25
Crystal size (mm)	0.32 × 0.27 × 0.23
No. of measured, independent and observed $[I > 2\sigma(I)]$ reflections	78 565, 9776, 5121
R_{int}	0.061
D_{cal} (Mg m^{-3})	1.272
$R[F^2 > 2\sigma(F^2)]$, w$R(F^2)$, S	0.06, 0.218, 1.15
No. of reflections	9776
No. of parameters	388
Range of $h\ k\ l$	$h = -15 \rightarrow 15$ $k = -18 \rightarrow 19$ $l = -19 \rightarrow 19$
θ range for data collection (°)	1.4–12.8
$\Delta\rho_{max}$, $\Delta\rho_{min}$ (e Å^{-3})	0.63, − 0.59

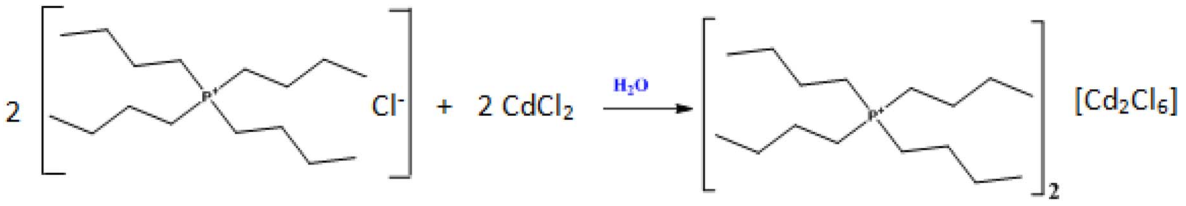

2.2. Single-crystal structure determination

A single crystal of bis(tetrabutylphosphonium) hexachlorodicadmate with dimensions of *ca.* 0.32 × 0.27 × 0.23 mm was selected and used for the single crystal diffraction experiment. Data-sets of $[(C_4H_9)_4P]_2Cd_2Cl_6$ compound were collected using a Bruker APEX-II Quazar diffractometer (4 circle Kappa goniometer) equipped with a CCD detector (Mo-Kα radiation, $\lambda = 0.71073$ Å) at 296 K. The empirical absorption correction was based by multi-scan method implemented in SADABS.[41] The structure solutions were obtained by direct methods, developed by successive difference Fourier synthesis and refined by full-matrix least-squares on all $|F|^2$ data using SHELX program[42] suite in WinGX software package.[43] The crystal structure was solved in the triclinic system with $P\bar{1}$ space group and $Z = 2$. All non-hydrogen atoms positions have been refined anisotropically whereas hydrogen atoms of the organic molecules have been geometrically constrained (HFIX options). The pertinent experimental details of the structure determination of the new compound are presented in Table 1. The interatomic distances and angles are listed in Tables 2 and 3. Figures of molecular structure were prepared using the graphical program Diamond.[44]

2.3. Hirshfeld surface

The Molecular Hirshfeld surfaces have been defined as the volume of space where molecule electron density exceeds that from all neighboring molecules[45,46] and generated by means of the Crystal Explorer package using the CIF file format.[47] For each point on the iso-surface two different types of distances are defined: one is d_e which is the distance to the nearest atoms outside and d_i, which is the distance to the nearest nucleus inside the surface, are readily defined. The normalized contact distance (d_{norm}) based on both d_e and d_i was given by the following equation:

$$d_{norm} = \frac{d_i - r_i^{vdw}}{r_i^{vdw}} + \frac{d_e - r_e^{vdw}}{r_e^{vdw}} \tag{1}$$

with $r_i$vdw and $r_e$vdw are the van der Waals radii of the atoms.

The value of d_{norm} was displayed using a red–white–blue color scheme corresponding to negative values (red regions) for shorter contacts, zero (white regions) for contacts around the van der Waals separation and positive (blue regions) for longer contacts. In addition, the combination of d_e and d_i in the form

Table 2 Bond lengths (Å) and angles (°) of $[Cd_2Cl_6]^{2-}$ [a]

Lengths (Å)		Angles (°)	
Cd1–Cl3	2.380 (2)	Cl3–Cd1–Cl2	116.59 (8)
Cd1–Cl2	2.385 (2)	Cl3–Cd1–Cl1	112.66 (9)
Cd1–Cl1	2.518 (2)	Cl2–Cd1–Cl1	110.99 (9)
Cd1–Cl1^{i}	2.520 (2)	Cl3–Cd1–Cl1^{i}	111.06 (9)
Cd2–Cl6	2.386 (2)	Cl2–Cd1–Cl1^{i}	112.06 (8)
Cd2–Cl5	2.391 (2)	Cl1–Cd1–Cl1^{i}	90.61 (6)
Cd2–Cl4^{i}	2.511 (3)	Cl6–Cd2–Cl5	116.17 (8)
Cd2– Cl4^{ii}	2.524 (3)	Cl6–Cd2–Cl4	111.72 (1)
		Cl5–Cd2–Cl4	113.84 (1)
		Cl6–Cd2–Cl4^{ii}	110.83 (1)
		Cl5–Cd2–Cl4^{ii}	111.33 (1)
		Cl4–Cd2–Cl4^{ii}	90.04 (9)
		Cd1–Cl1–Cd1^{i}	89.39 (6)
		Cd2–Cl4–Cd2^{ii}	89.97 (9)

[a] Symmetry codes: (i) $-x + 1, -y + 1, -z + 1$; (ii) $-x, -y + 2, -z + 2$.

of a 2D fingerprint plot presents the proportions of these intermolecular interactions.[48]

2.4. Thermal analysis

DSC measurement was performed using PerkinElmer DSC 4000 calorimeter, under the following conditions: sample weight *ca.* 12 mg with the nitrogen gas (N_2) at 20.0 ml min^{-1} in the temperature range of 300 to 440 K.

2.5. Powder X-ray diffraction

Powder X-ray diffraction (PXRD) measurements at 300 K and 370 K were performed on a BRUKER D8 ADVANCE diffractometer, equipped with an LYNXEYE XE-T detector and using a Cu-Kα radiation source. The long fine focus (LFF) ceramic tube operated at 40 kV and 40 mA. The calculated PXRD patterns were generated by PLATON[49] and FOX[50] programs for 300 and 370 K, respectively.

2.6. Optical observations

Optical observations were taken on powder at room temperature using a Shimadzu (UV 3101 PC) UV-vis-NIR scanning spectrophotometer with a wavelength radiation varying from 200 to 800 nm to determine the band-gap energy of the title compound. The apparatus lets the measure of the absorbance and the reflectance by the external mode employing an integrating sphere and a xenon lamp and $BaSO_4$ powder to register the reference signal.

2.7. Electrical studies

Electrical measurements of the $[(C_4H_9)_4P]_2Cd_2Cl_6$ material were performed using a Solartron 1260 impedance analyzer. Silver films were placed on two opposite parallel faces of the pellet. Therefore, a configuration of a plate capacitor was obtained. The measurements were carried out over a wide range of frequency [40–106 Hz] and temperature [313–368 K].

Table 3 Bond lengths (Å) and angles (°) of $[(C_4H_9)_4P]^+$

Lengths (Å)		Angles (°)	
P1–C1	1.78 (1)	C1–P1–C5	113.5 (5)
P1–C5	1.78 (9)	C1–P1–C13	110.0 (5)
P1–C13	1.81 (1)	C5–P1–C13	103.2 (5)
P1–C9	1.80 (1)	C1–P1–C9	105.9 (5)
P2–C25	1.78 (1)	C13–P1–C9	114.6 (6)
P2–C21	1.78 (1)	C25–P2–C21	111.5 (6)
P2–C17	1.78 (1)	C25–P2–C17	105.7 (7)
P2–C29	1.79 (1)	C21–P2–C17	108.4 (7)
C5–C6	1.44 (1)	C25–P2–C29	106.6 (6)
C9–C10	1.51 (2)	C21–P2–C29	111.0 (6)
C21–C22	1.44 (2)	C17–P2–C29	113.5 (7)
C1–C2	1.51 (2)	C6–C5–P1	115.1 (7)
C29–C30	1.47 (2)	C10–C9–P1	114.0 (8)
C25–C26	1.54 (2)	C22–C21–P2	114.9 (1)
C6–C7	1.57 (2)	C2–C1–P1	113.9 (8)
C17–C18	1.35 (2)	C30–C29–P2	118.0 (1)
C22–C23	1.51 (2)	C26–C25–P2	115.5 (8)
C2–C3	1.45 (2)	C5–C6–C7	115.5 (8)
C10–C11	1.46 (2)	C5–C6–C7	112.9 (1)
C26–C27	1.52 (2)	C18–C17–P2	121.1 (1)
C13–C14	1.38 (2)	C21–C22–C23	117.9 (2)
C3–C4	1.41 (2)	C3–C2–C1	117.9 (2)
C7–C8	1.48 (3)	C11–C10–C9	113.6 (1)
C14–C15	1.77 (3)	C27–C26–C25	113.3 (1)
C27–C28	1.31 (3)	C14–C13–P1	120.0 (1)
C30–C31	1.60 (3)	C4–C3–C2	116.8 (2)
C16–C15	1.32 (2)	C8–C7–C6	114.8 (2)
C31–C32	1.27 (2)	C17–C18–C19	116.4 (2)
C23–C24	1.30 (2)	C20–C19–C18	112 (2)
C18–C19	1.53 (2)	C12–C11–C10	109.2 (2)
C19–C20	1.43 (3)	C13–C14–C15	110.9 (1)
C11–C12	1.48 (3)	C28–C27–C26	121 (3)
		C29–C30–C31	109.4 (2)
		C32–C31–C30	99 (2)
		C24–C23–C22	131 (3)
		C16–C15–C14	97 (3)

3. Results and discussion

3.1. Description of the crystal structure

The structural study of $[(C_4H_9)_4P]_2Cd_2Cl_6$ compound showed that the asymmetric unit contains two tetrabutylphosphonium cations $[(C_4H_9)_4P]^+$ and two halfs $[Cd_2Cl_6]^{2-}$ anion (Fig. 1). The projection of the atomic arrangement of bis(tetrabutylphosphonium)hexachlorodicadmate along the *c*-axis reveals that the inorganic entities $[Cd_2Cl_6]^{2-}$ are placed in cavities formed by pairs of $[(C_4H_9)_4P]^+$, where each anion is formed by two $[CdCl_4]^{2-}$ tetrahedra sharing one common edge, which lead to the Cd_2Cl_6 clusters (Fig. 2). This structure exhibits similarities to analogous compounds such as $[(C_3H_7)_4P]_2Cd_2Br_6$ (ref. 51) and $[N(C_3H_7)_4]_2Cd_2Cl_6$.[52] All are centrosymmetric with $P\bar{1}$ space group. Apart the electrostatic interactions, extensive bonds of C–H⋯Cl type play a key role to maintain the cohesion between the different organic and inoganic entities which forming a three-dimensional supramolecular network (Fig. 3).

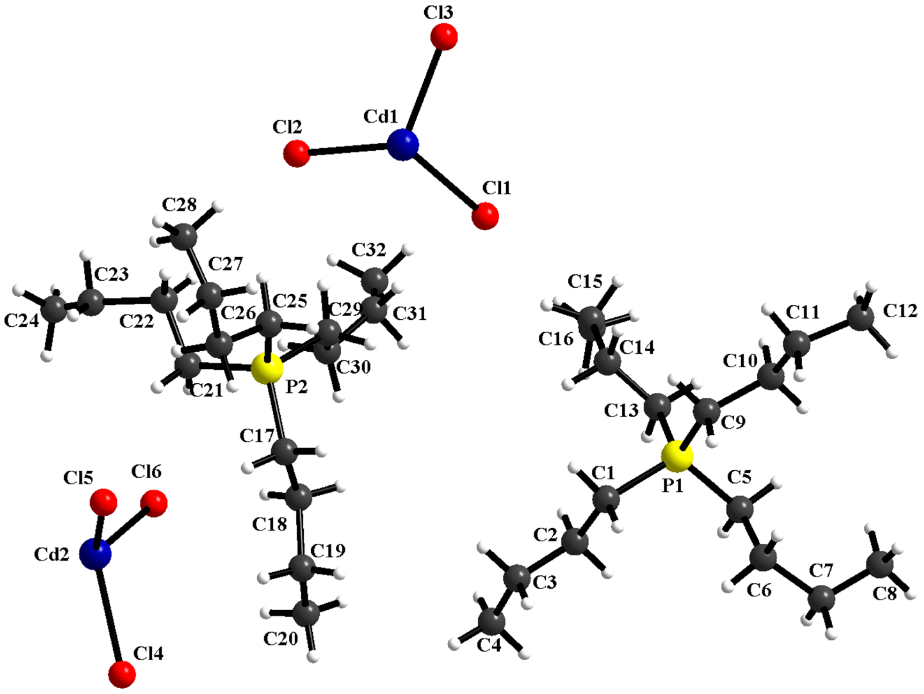

Fig. 1 The asymmetric unit of $[(C_4H_9)_4P]_2Cd_2Cl_6$.

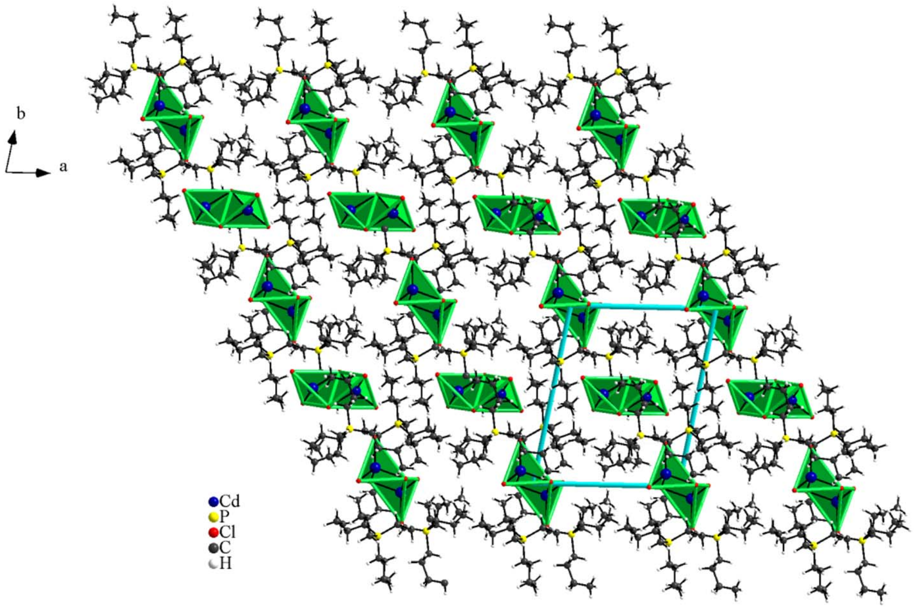

Fig. 2 Projection of the atomic arrangement of $[(C_4H_9)_4P]_2Cd_2Cl_6$ in the (a, b) plane.

3.2. Hirshfeld surface analysis

In the present paper, we studied Hirshfeld surfaces in order to identify intermolecular interactions and the environments of the components in the unit cell. The d_{norm} and 2D fingerprint plots mapped on Hirshfeld surface are shown in Fig. 4. The two-dimensional fingerprint plot reveals that the H···H and Cl···H/H···Cl intermolecular interactions were the most abundant in the crystal packing (56.0% and 42.6%, respectively) which indicated that van der Waals forces exert an important influence on the stabilization of the packing in the crystal structure. Other intercontacts; Cd···H/H···Cd are less contributed to the Hirshfeld surfaces (1.4%).

3.3. Thermal characterization

The thermal changes of materials include different phenomena like crystallization, melting, glass transition, *etc.*, which can be

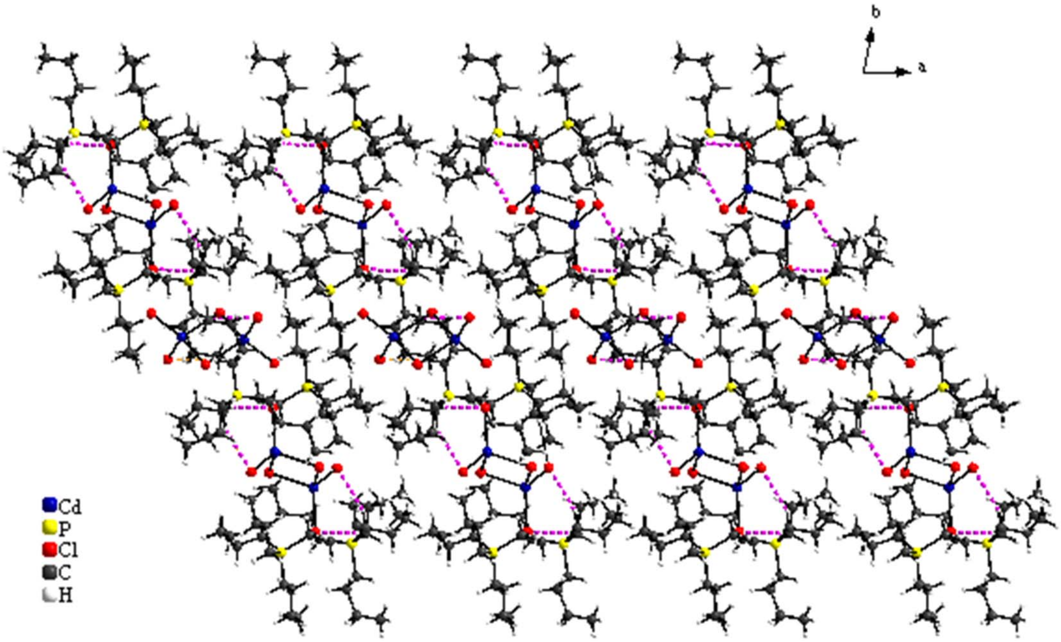

Fig. 3 Crystal packing of the title compound. Dashed lines indicate C⋯H–Cl bonds.

studied with the differential scanning calorimetry under a flux of an inert gas (argon, nitrogen), in order to avoid the reaction of the material with the atmosphere. Fig. 5 shows the DSC runs for $[(C_4H_9)_4P]_2Cd_2Cl_6$ compound in the heating temperature range [300–440 K]. The obtained thermogram clearly reveals the existence of only endothermic peak located around 348 K, which can be attributed to a phase transition. The obtained enthalpy and entropy of the phase transition are equal to 13.5278 J g^{-1} and 0.0388 J g^{-1} K^{-1}, respectively. This phase transition is comparable to that observed in $[(C_4H_9)_4P]SbCl_4$.[53]

3.4. X-ray powder diffraction studies

Fig. S1† shows the thermal evolution of the PXRD patterns of $[(C_4H_9)_4P]_2Cd_2Cl_6$ at 300 K and 370 K, respectively. The PXRD pattern collected above 348 K is completely different from that below this temperature. This change is attributed to the first order structural phase transition detected by DSC. It should be noted that the calculated PXRD patterns for 300 and 370 K are identical to those determined experimentally (Fig. S1†). This result is in agreement with a monophasic crystalline powder whether before or after the detected transition.

3.5. Optical properties

The absorption spectrum of the studied compound measured at room temperature is given in Fig. 6. The UV absorption spectrum of $[(C_4H_9)_4P]_2Cd_2Cl_6$ shows two strong absorptions in the region between 200 to 350 nm, and no obvious absorption from 350 to 800 nm (see Fig. 6), suggesting that the material has a wide transparent region. The first peak is attributed to the excitation of free electron hole pairs within the $[Cd_2Cl_6]^{2-}$ inorganic anion, which is very similar to others organic–inorganic hybrid compounds.[54,55] Under excitation, an electron is excited from the valence band (VB) to the conduction band (CB), leaving a hole in the VB The electron's transition back to the ground, which is the recombination of the electron and hole, yields an absorption band centered at 348 nm. The optical band gap (E_g) for bis(tetrabutylphosphonium) hexachlorodicadmate can be determined by extrapolation from the absorption edge which is given by the following equation.[56]

$$(F(R)h\nu)^n = A(h\nu - E_g) \quad (2)$$

where R is the absolute reflectance of the sample, A is a constant that depends on the energy, $h\nu$ is the energy of the incident photon and n is the constant that takes different values depending on the type of the electronic transition. The band gap of this material is approximately 2.65 eV (see Fig. 6) which indicates its semi-conducting behavior. This optical band gap value is similar to those of $[(C_4H_9)_4P]SbCl_4$ (ref. 53) and $(C_5H_8N_3)_2[BiCl_5]$[57] molecular crystals which are a good semiconductors.

3.6. Electrical properties

3.6.1. Nyquist plots. The Nyquist plots ($-Z''$ *vs.* Z') of the title compound at some temperatures was shown in Fig. 7. These plots prove that there are typical semi-circles, whose center lies below the abscise axis and which become clearly smaller as the temperature increases; this indicates a non-Debye type of relaxation.[58] These curves were fitted using the *Z*-view software. The best fit is obtained when employing an equivalent circuit consists of a parallel contribution of grain resistance (R1) and constant phase element (CPE1) (insert in Fig. 7).

The frequency dependence of Z'' and Z' at some temperatures for $[(C_4H_9)_4P]_2Cd_2Cl_6$ sample are presented in Fig. 8. The good

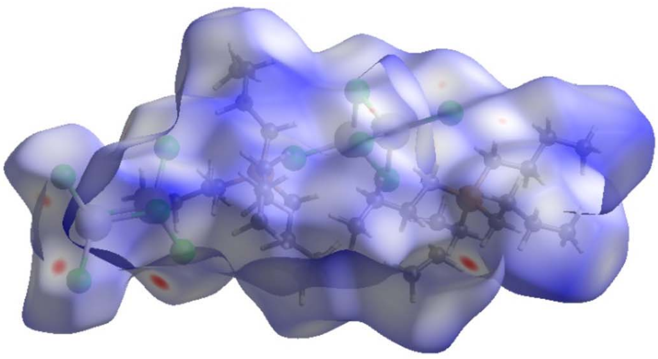

d_{norm}

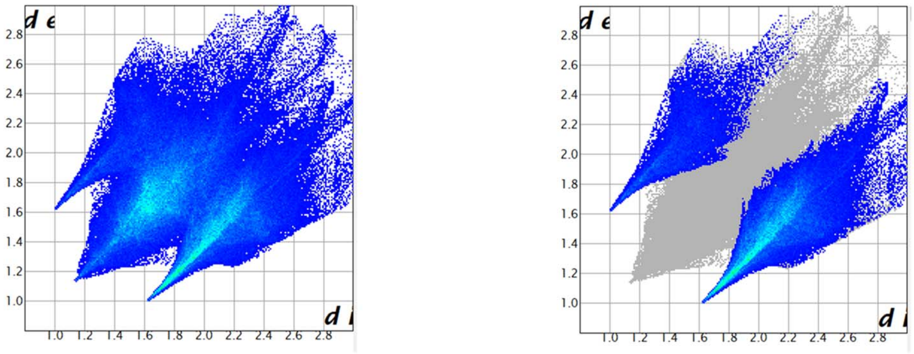

All interactions (100 %)

Cl···H/H···Cl (42.6) %)

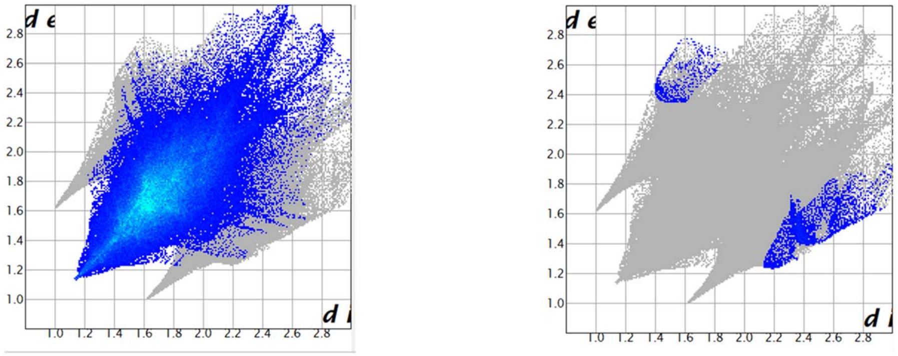

H···H (56.0 %)

Cd···H/H···Cd (1.4 %)

Fig. 4 Hirshfeld surfaces of $[(C_4H_9)_4P]_2Cd_2Cl_6$: d_{norm} and the two-dimensional fingerprint plots.

conformity of the calculated lines with experimental indicates that the suggested equivalent circuit describes the crystal electrolyte interface reasonably well.

We clearly observe that the amplitude of the real parts Z', here represents the electrical resistance, decreases with increase in frequency and temperature. This phenomenon

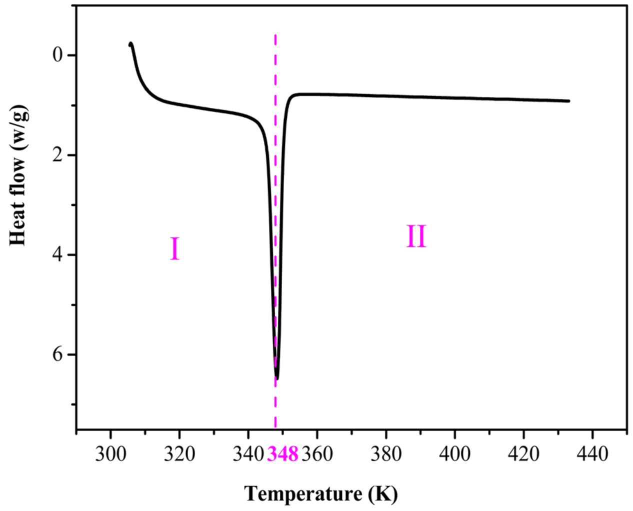

Fig. 5 Differential scanning calorimetry of $[(C_4H_9)_4P]_2Cd_2Cl_6$.

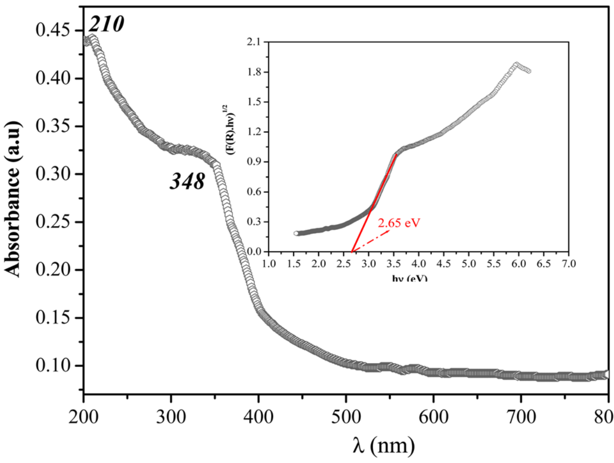

Fig. 6 UV-vis diffuse reflectance spectroscopy plots for bis(tetrabutylphosphonium) hexachlorodicadmate(II).

involves the negative temperature coefficient of resistance (NTCR) in $[(C_4H_9)_4P]_2Cd_2Cl_6$ compound. At higher frequencies, the Z' values for all temperatures move towards the same point, suggesting a probable release of space charge and consequence lower energy barrier properties.[59]

Analyzing the variation of Z'' with the angular frequency one can observe the appearance of a single peaks at a particular frequency, a decrease in the height of the peaks with the increase of the temperature. Further, we have noticed a peak broadening with decreasing of the value of Z''_{max} which suggests an increasing loss in the resistive properties of the sample.[60] The relaxation peak shifts to high frequency regions indicating the accumulation of space charge in the material. Similar type of behavior is also observed in other studied material.[61]

3.6.2. Conductivity study.

The variation of Alternating Current conductivity (AC conductivity: σ_{AC}) depending on the angular frequency at various temperatures of $[(C_4H_9)_4P]_2Cd_2Cl_6$ was described in Fig. 9. It is obvious from this figure that each

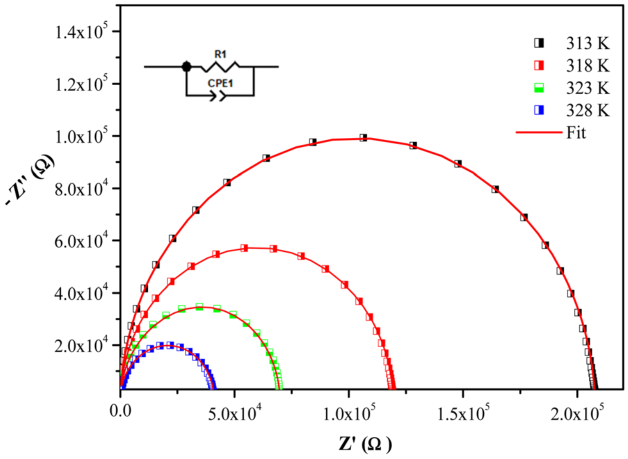

Fig. 7 Complex impedance spectra at some temperatures with equivalent circuit.

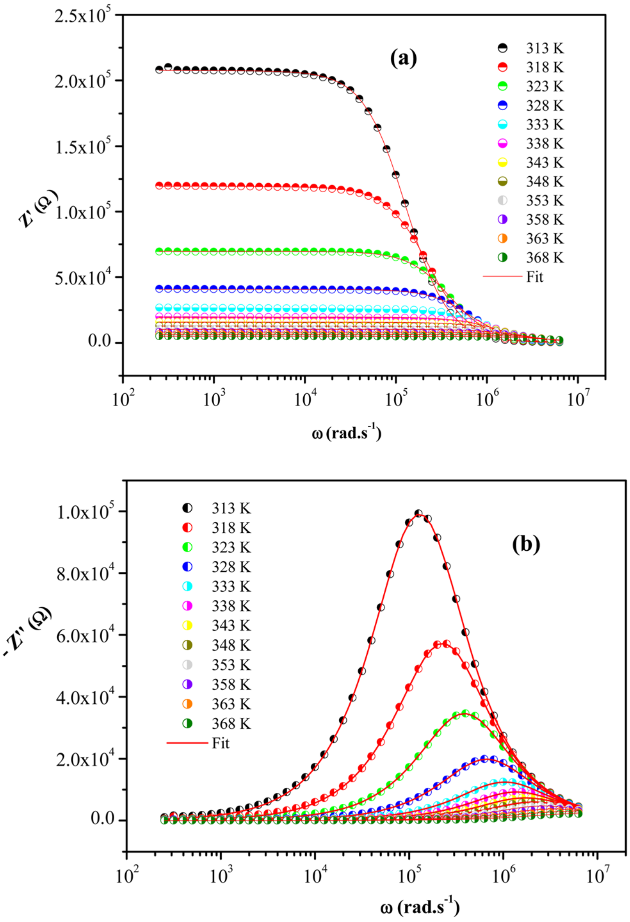

Fig. 8 The frequency dependence of Z' (a) and Z'' (b) at different temperatures for $[(C_4H_9)_4P]_2Cd_2Cl_6$ crystal.

curve constitutes a frequency-independent domain next to a dispersive region; the former represents the Direct Current conductivity (DC conductivity: σ_{DC}) whereas the latter refers to alternating conductivity denoted as σ_{AC}. The conductivity of this compound responds to the frequency in two different ways

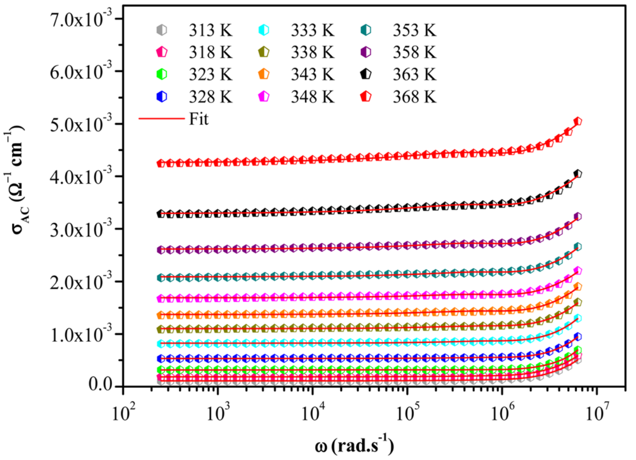

Fig. 9 Frequency dependence of AC conductivity at various temperatures.

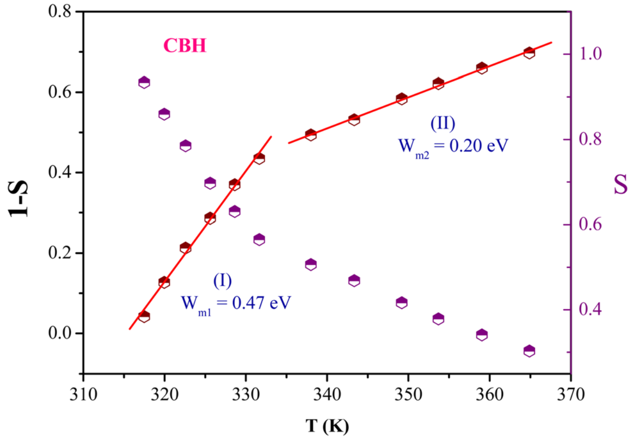

Fig. 10 Thermal variation of exponent "S" and "1-S" for $[(C_4H_9)_4P]_2Cd_2Cl_6$.

depending on the temperature. The nature of AC conductivity with frequency shows that it follows universal Johnscher's power law, given by the following equation:

$$\sigma_{AC} = \sigma_{DC} + A\omega^{S} \tag{3}$$

where A is a constant, ω is the angular frequency and S is an exponent expressing the degree of interaction between the mobile charge and its surrounding.[62]

Fig. S2† shows the thermal evolution of the conductivity as a function of $(1000/T)$ in the title compound. The phase transition observed in the calorimetric study is confirmed by a change of the slope around 348 K. Two regions are observed in the ranges from 313 to 338 K and from 343 to 368 K, indicating an Arrhenius-type behavior.[63]

$$\sigma T = A\,\exp\left(-\frac{E_a}{K_B T}\right) \tag{4}$$

where A is the pre-exponential factor, E_a is the activation energy and k_B is the Boltzmann's constant. The obtained activation energies ranged from 0.8 to 0.5 eV in region (I) [313–338 K] and region (II) [343–368 K], respectively.

In this material, the dominant conduction mechanism according to which σ_{AC} occurs will be discussed in this part. Thermal variation of exponent S and 1-S are reported in Fig. 10.

It is found that S decreases with the increasing of temperature. Comparing this result with those of $[(C_3H_7)_4P]_2Cd_2Br_6$ (ref. 51) and $[(C_4H_9)_4\ P]SbCl_4$ (ref. 53) compounds it can be concluded that the correlated barrier hopping (CBH) model is also the most probable conduction mechanism for this compound.[64]

In the CBH model, the exponent S is defined by the following expression:[65]

$$S = 1 - \left(\frac{6k_B T}{W_M}\right) \tag{5}$$

where W_M is the maximum barrier height, the value of W_M obtained from the linear fit of the straight line 1-S as function of temperature (Fig. 10) is equal to 0.47 eV and 0.20 eV in regions (I) and (II), respectively. These values are approximately a half of the activation energies $\left(W_M \sim \frac{E_a}{2}\right)$ for both regions. Generally, if $W_M = \frac{E_a}{2}$, the bipolaron hopping is the dominating conduction mechanism and if $W_M = \frac{E_a}{4}$, the single polaron is dominating,[66] which can suggest that the bipolaron hopping is the dominating conduction mechanism in the title compound.

In order to verify the validity of the CBH model on this material, the experimental curves of $\ln(\sigma_{AC})$ *versus* $(1000/T)$ for the following frequencies 10^6 Hz, 5.01 10^5 Hz and 40 Hz; have been fitted using eqn (6). Fig. S3† clearly shows that the theoretical calculations of the conductivity at different frequencies match up well with the experimental data.

$$\sigma_{AC} = \frac{n\pi^3 N N_p \varepsilon_0 \varepsilon' \omega R_\omega{}^6}{24} \tag{6}$$

n is the number of polarons involved in the hopping process, N is the density of localized states where carriers exist, N_p is the density of localized states where the carriers hop, ε_0 is the dielectric constant of the free space and ε' dielectric constant of the material. By comparing with similar compounds, we can deduce that the conductivity in this sample is ensured by the contribution of the movements of cationic and anionic parts.[67]

3.6.3. Modulus analysis. We have also investigated the electrical modulus to study the relaxation mechanism in hybrid material $[(C_4H_9)_4P]_2Cd_2Cl_6$. Fig. 11 illustrated the variation of imaginary part of electric modulus M'' with frequency at different temperatures. The graph shows a well-defined maximum (M''_{max}) with a characteristic relaxation rate. The modulus peaks shift towards higher frequency side on increasing temperature, which indicates a correlation between the motions of mobile charge carriers in the sample. Indeed, the frequency region below the peak M''_{max} determines the range in which the charge carriers are mobile on long distances. However, the frequency regions above peak M''_{max} determine

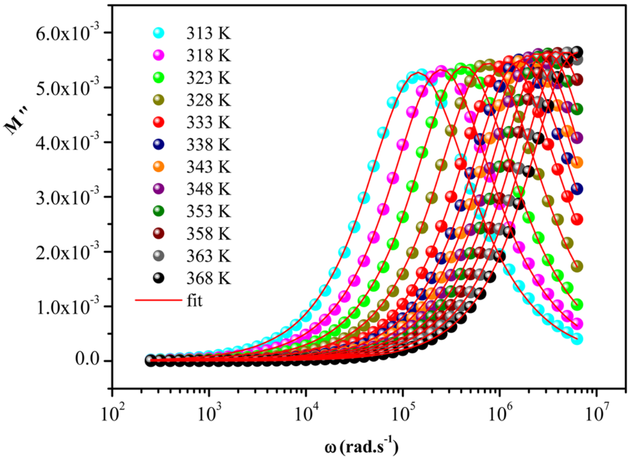

Fig. 11 Imaginary part of modulus as a function of frequency at different temperatures.

the range in which the carriers are confined to potential wells, being mobile on short distances.

The imaginary part of the modulus has been simulated with eqn (7) proposed by Bregman.[68]

$$M'' = \frac{M''_{\max}}{1-\beta+\left(\frac{\beta}{1+\beta}\right)\left[\beta\left(\frac{\omega_{\max}}{\omega}\right)+\left(\frac{\omega}{\omega_{\max}}\right)^{\beta}\right]} \qquad (7)$$

where $M''_{\max}$ and $\omega_{\max}$ are the peak maximum and the peak angular frequency of the imaginary part of the modulus, respectively and b is exponent. The value of β is positioned in the range $0 < \beta < 1$, which represents the deviation from the linear exponential.

The temperature dependence of β parameter extracted by fitting the curves of M'' is shown in Fig. S4.† In this figure, we observed that β increases linearly with increasing temperature and shows two regions with a change in the slope around 348 K in accordance with the temperature of phase transition determined by DSC measurement. Furthermore, at low temperature, the small values of β indicated that the coupling between charge carriers is more extended in this region. While, at high temperature, the greatest values of β are due to low interaction between the charges carriers which can be due to the increases of the distances between charge carries below the phase transition.[69]

3.6.4. Dielectric studies. The frequency dependence of the real ε' and imaginary ε'' parts of the dielectric permittivity for the studied material at different temperatures was described in Fig. 12a and b. These figures showed that the dielectric constant values (ε' and ε'') decreased with increasing frequencies. There is a sharp rise in the dielectric constant at low frequency and the shape of the rise changes with the temperature, due to the conducting ion motion. The high value of the dielectric constant reflects the effect of the space charge polarization and the conducting ionic motion. The high value of the dielectric constant at low frequency and the low value of this constant at high frequency indicate a large dielectric dispersion due to the Maxwell–Wagner type interfacial polarization.[70]

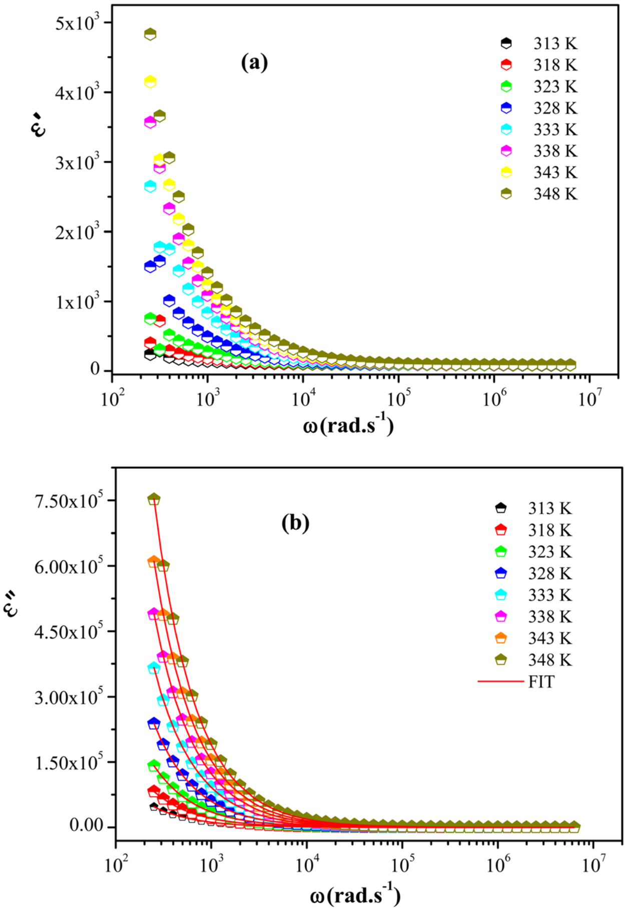

Fig. 12 Frequency dependence of ε' (a) and ε'' (b) at some temperatures.

4. Conclusion

In conclusion, a new organic-inorganic hybrid material $[(C_4H_9)_4P]_2Cd_2Cl_6$ has been successfully synthesized through simple slow evaporation method at 296 K. The single crystal diffraction shows that this sample crystallizes at room temperature in the triclinic system with $P\bar{1}$ centrosymmetric space group. The asymmetric unit of this crystal revealed two tetrabutylphosphonium cations $[(C_4H_9)_4P]^+$ and two halfs of $[Cd_2Cl_6]^{2-}$ anion, whose crystal structure is stabilized by electrostatic interactions and C–H···Cl bonds type. Hirshfeld surface fingerprint plots showed different types of intermolecular interactions including hydrogen bonding. The DSC measurement indicated the presence of one endothermic peak at 348 K which is attributed to a phase transition. The optical properties showed that the title compound has a semi-conducting character for which the gap energy is 2.65 eV. Furthermore, the Nyquist plots exhibit a non-Debye relaxation behavior. The AC conductivity, found to obey the universal power law S. The decrease of the frequency exponent S with temperature suggested that the correlated barrier hopping (CBH) model is the probable mechanism for electrical transport phenomenon. Besides, the high values of the dielectric constant (ε' and ε'') at low frequency are explained using the Maxwell–Wagner polarization model.

Conflicts of interest

The authors declare no competing financial interest.

Acknowledgements

The authors extend their appreciation to the deanship of scientific research at King Khalid University for funding this work through large group research project under grant number RGP2/440/44.

References

1 P. S. Weiss, The Supramolecular Chemistry of Organic-inorganic Hybrid Materials, *J. Am. Chem. Soc.*, 2010, **132**, 10954.

2 S. Jeong, D. Kim and J. Moon, Ink-Jet-Printed Organic–Inorganic Hybrid Dielectrics for Organic Thin-Film Transistors, *J. Phys. Chem. C*, 2008, **112**, 5245–5249.

3 D.-B. Mitzi, Synthesis, Crystal Structure, and Optical and Thermal Properties of $(C_4H_9NH_3)_2MI_4$ (M = Ge, Sn, Pb), *Chem. Mater.*, 1996, **8**, 791–800.

4 M. Era, S. Morimoto, T. Tsutsui and S. Saito, Organic-inorganic heterostructure electroluminescent device using a layered perovskite semiconductor $(C_6H_5C_2H_4NH_3)_2PbI_4$, *Appl. Phys. Lett.*, 1994, **65**, 676–678.

5 F. Witt, M. Kruszynska, H. Borchert and J. Parisi, Charge Transfer Complexes in Organic-Inorganic Hybrid Blends for Photovoltaic Applications Investigated by Light-Induced Electron Spin Resonance Spectroscopy, *J. Phys. Chem. Lett.*, 2010, **20**, 2999–3003.

6 H.-J. Bolink, H. Brine, E. Coronado and M. Sessolo, Ionically Assisted Charge Injection in Hybrid Organic-Inorganic Light-Emitting Diodes, *ACS Appl. Mater. Interfaces*, 2010, **2**, 2694–2698.

7 J.-J. Wang, Y.-Q. Wang, F.-F. Cao, Y.-G. Guo and L.-J. Wan, Synthesis of Monodispersed Wurtzite Structure $CuInSe_2$ Nanocrystals and Their Application in High-Performance Organic−Inorganic Hybrid Photodetectors, *J. Am. Chem. Soc.*, 2010, **132**, 12218–12221.

8 A. Corma, U. Díaz, T. García, G. Sastre and A. Velty, Multifunctional Hybrid Organic-Inorganic Catalytic Materials with a Hierarchical System of Well-Defined Micro- and Mesopores, *J. Am. Chem. Soc.*, 2010, **132**, 15011–15021.

9 S.-A. Veldhuis, P. P. Boix, N. Yantara, M. Li, T. C. Sum, N. Mathews and S. G. Mhaisalkar, Perovskite Materials for Light-Emitting Diodes and Lasers, *Adv. Mater.*, 2016, **28**, 6804–6834.

10 S.-D. Wolf, J. Holovsky, S.-J. Moon, P. Löper, B. Niesen, M. Ledinsky, F.-J. Haug, J.-H. Yum and C. Ballif, Organometallic Halide Perovskites: Sharp Optical Absorption Edge and Its Relation to Photovoltaic Performance, *J. Phys. Chem. Lett.*, 2014, **5**, 1035–1039.

11 C. Wehrenfennig, G. E. Eperon, M. B. Johnston, H. J. Snaith and L. M. Herz, High Charge Carrier Mobilities and Lifetimes in Organolead Trihalide Perovskites, *Adv. Mater.*, 2014, **26**, 1584–1589.

12 A. Walsh, D. O. Scanlon, S. Chen, X. G. Gong and S. -H. Wei, Self-Regulation Mechanism for Charged Point Defects in Hybrid Halide Perovskites, *Angew. Chem., Int. Ed.*, 2015, **54**, 1791–1794.

13 A.-T. Barrows, A.-J. Pearson, C. K. Kwak, A. D. F. Dunbar, A. R. Buckley and D. G. Lidzey, Efficient planar heterojunction mixed-halide perovskite solar cells deposited *via* spray-deposition, *Energy Environ. Sci.*, 2014, **7**, 2944–2950.

14 X. Lin, D. Cui, X. Luo, C. Zhang, Q. Han, Y. Wang and L. Han, Efficiency progress of inverted perovskite solar cells, *Energy Environ. Sci.*, 2020, **13**, 3823–3847.

15 M.-R. Filip, S. Hillman, A. A. Haghighirad, H. J. Snaith and F. Giustino, Band Gaps of the Lead-Free Halide Double Perovskites $Cs_2BiAgCl_6$ and $Cs_2BiAgBr_6$ from Theory and Experiment, *J. Phys. Chem. Lett.*, 2016, **7**, 2579–2585.

16 E.-T. McClure, M. R. Ball, W. Windl and P. M. Woodward, Cs_2AgBiX_6 (X = Br, Cl): New Visible Light Absorbing, Lead-Free Halide Perovskite Semiconductors, *Chem. Mater.*, 2016, **28**, 1348–1354.

17 A. H. Slavney, T. H. Aaron, M. Lindenberg and H. I. Karunadasa, A Bismuth-Halide Double Perovskite with Long Carrier Recombination Lifetime for Photovoltaic Applications, *J. Am. Chem. Soc.*, 2016, **138**, 2138–2141.

18 F. Wei, Z. Deng, S. Sun, F. Xie, G. Kieslich, D. M. Evans, M. l A. Carpenter, P. D. Bristowe and A. K. Cheetham, The synthesis, structure and electronic properties of a lead-free hybrid inorganic–organic double perovskite $(MA)_2KBiCl_6$ (MA = methylammonium), *Mater. Horiz.*, 2016, **3**, 328–332.

19 X.-G. Zhao, J.-H. Yang, Y. Fu, D. Yang, Q. Xu, L. Yu, S.-H. Wei and L. Zhang, Design of Lead-Free Inorganic Halide Perovskites for Solar Cells *via* Cation-Transmutation, *J. Am. Chem. Soc.*, 2017, **139**, 2630–2638.

20 X.-G. Zhao, D. Yang, Y. Sun, T. Li, L. Zhang, L. Yu and A. Zunger, Cu–In Halide Perovskite Solar Absorbers, *J. Am. Chem. Soc.*, 2017, **139**, 6718–6725.

21 T. Nakajima and K. Sawada, Discovery of Pb-Free Perovskite Solar Cells *via* High-Throughput Simulation on the K Computer, *J. Phys. Chem. Lett.*, 2017, **8**, 4826–4831.

22 N. Saito, D. Nishiyama, Y. Matsushita, Y. Wada, S. Cordier, T. Ohsawa, F. Grasset and N. Ohashi, Reentrant structural and optical properties of organic–inorganic hybrid metal cluster compound $((n\text{-}C_4H_9)_4N)_2[Mo_6Br^{i}{}_8Br^{a}{}_6]$, *CrystEngComm*, 2022, **24**, 465–470.

23 M. Wilmet, C. Lebastard, F. Sciortino, C. C-Zerbino, L. MacAleese, F. Chirot, Ph. Dugourd, F. Grasset, Y. Matsushita, T. Uchikoshi, K. Ariga, P. Lemoine, A. Renaud, K. Costuas and S. Cordier, Revisiting properties of edge-bridged bromide tantalum clusters in the solid-state, in solution and vice versa: an intertwined experimental and modelling approach, *Dalton Trans.*, 2021, **50**, 8002–8016.

24 Z. Xiao, K.-Z. Du, W. Meng, J. Wang, D. B. Mitzi and Y. Yan, Intrinsic Instability of $Cs_2In(I)M(III)X_6$ (M = Bi, Sb; X = Halogen) Double Perovskites: A Combined Density Functional Theory and Experimental Study, *J. Am. Chem. Soc.*, 2017, **139**, 6054–6057.

25 J. Leveillee, G. Volonakis and F. Giustino, Phonon-Limited Mobility and Electron–Phonon Coupling in Lead-Free Halide Double Perovskites, *J. Phys. Chem. Lett.*, 2021, **12**, 4474–4482.

26 M. R. Filip and F. Giustino, Computational Screening of Homovalent Lead Substitution in Organic–Inorganic Halide Perovskites, *J. Phys. Chem. C*, 2016, **120**, 166–173.

27 R. J. Sutton, M. R. Filip, A. A. Haghighirad, N. Sakai, B. Wenger, F. Giustino and H. J. Snaith, Cubic or Orthorhombic? Revealing the Crystal Structure of Metastable Black-Phase $CsPbI_3$ by Theory and Experiment, *ACS Energy Lett.*, 2018, **3**, 1787–1794.

28 G. Volonakis, M. R. Filip, A. A. Haghighirad, N. Sakai, B. Wenger, H. J. Snaith and F. Giustino, Lead-Free Halide Double Perovskites *via* Heterovalent Substitution of Noble Metals, *J. Phys. Chem. Lett.*, 2016, **7**, 1254–1259.

29 V. d. Z. Bermudez, L. D. Carlos, M. C. Duarte, M. M. Silva, C. J. Silva, M. J. Smith, M. Assuncao and L. Alcacer, A novel class of luminescent polymers obtained by the sol–gel approach, *J. Alloys Compd.*, 1998, **275–277**, 21–26.

30 L. D. Carlos, R. A. S. Ferreira, V. d. Z. Bermudez and S. J. L. Ribeiro, Full-Color Phosphors from Amine-Functionalized Crosslinked Hybrids Lacking Metal Activator Ions, *Adv. Funct. Mater.*, 2001, **2**, 111–115.

31 Y. Kato, D. Ichii, K. Ohashi, H. Kunugita, K. Ema, K. Tanaka, T. Takahashi and T. Kondo, Extremely large binding energy of biexcitons in an organic–inorganic quantum-well material $(C_4H_9NH_3)_2PbBr_4$, *Solid State Commun.*, 2003, **128**, 15–18.

32 A. E. Korashy and M. G. BriK, Crystal growth, spectroscopic and crystal field studies of $[N(CH_3)_4]_2MnCl_4$ and $[N(CH_3)_4]_2CoCl_4$ single crystals in the paraelectric phase, *Solid State Commun.*, 2005, **135**, 298–303.

33 A. Ben Rhaiem, F. Hlel, K. Guidara and M. Gargouri, Dielectric relaxation and ionic conductivity studies of [N(CH3)4]2Cu0.5Zn0.5Cl4, *J. Alloys Compd.*, 2008, **463**, 440–445.

34 A. B. Corradi, A. M. Ferrari and G. C. Pellacani, Organic-inorganic composite materials: structural archetypes of linear polymeric chlorocadmates (II), *Inorg. Chim. Acta*, 1998, **272**, 252–260.

35 F. Neve, O. Francescangeli and A. Crispini, Crystal architecture and mesophase structure of long-chain N-alkylpyridinium tetrachlorometallates, *Inorg. Chim. Acta*, 2002, **338**, 51–58.

36 S. Kuriyama, Y. Inomata, Y. Arai and F. S. Howell, Characterization and crystal structure of cadmium (II) halide complexes with amino acids and their derivatives: VII. Crystal structures of aquadibromo (3-aminopropanoic acid) cadmium (II), dichloro (4-aminobutanoic acid) cadmium (II), diaquabis (aminohexanoic acid) cadmium(II) tetrachlorocadmium(II), and dibromo (azetidine-3-carboxylic acid) cadmium (II), *J. Inorg. Biochem.*, 2006, **100**, 1299–1307.

37 A. Lamhamdi, E. Mejdoubi, K. Fejfarova, M. Dušek and B. El Bali, Poly [ethane-1,2-diammonium tetra-μ-chlorido-cadmate(II)], *Acta Crystallogr., Sect. E: Crystallogr. Commun.*, 2009, **65**, m215–m216.

38 C. J. Adams, M. A. Kurawa and A. G. Orpen, Coordination Chemistry in the Solid State: Reactivity of Manganese and Cadmium Chlorides with Imidazole and Pyrazole and Their Hydrochlorides, *Inorg. Chem.*, 2010, **49**, 10475–10485.

39 A. G-Raso, J. J. Fiol, A. Tasada, F. M. Albertí, F. Bádenas, X. Solans and M. F- Bardia, N9, N9′-polymethylene-bisadenine complexes with d10 metal ions, *Polyhedron*, 2007, **26**, 949–957.

40 S. Liu, X. Fang, B. Lu and D. Yan, Wide range zero-thermal-quenching ultralong phosphorescence from zero-dimensional metal halide hybrids, *Nat. Commun.*, 2020, **11**, 1–9.

41 G. M. Sheldrick, *SADABS, Program for Empirical Absorption Correction of Area Detector Data*, University of Gottingen, Germany, 1996, p. 467.

42 G. M. Sheldrick, A short history of SHELX, *Acta Crystallogr., Sect. A: Found. Crystallogr.*, 2008, **64**, 112–122.

43 L. J. Farrugia, WinGXsuite for small-molecule single-crystal crystallography, *J. Appl. Crystallogr.*, 1999, **32**, 837–838.

44 K. Brandenburg and M. Berndt, *Diamond Crystal impact Gb R*, Bonn, Germany, version 2.1.b, 1999.

45 O. S. Urgut, I. I. Ozturk, C. N. Banti, N. Kourkoumelis, M. Manoli, A. J. Tasiopoulos and S. K. Hadjikakou, New antimony (III) halide complexes with dithiocarbamate ligands derived from thiuram degradation: The effect of the molecule's close contacts on *in vitro* cytotoxic activity, *Mater. Sci. Eng. C*, 2015, **58**, 396–408.

46 O. S. Urgut, I. I. Ozturk, C. N. Banti, N. Kourkoumelis, M. Manoli, A. J. Tasiopoulos and S. K. Hadjikakou, Addition of tetraethylthiuram disulfide to antimony(III) iodide; synthesis, characterization and biological activity, *Inorg. Chim. Acta*, 2016, **443**, 141–150.

47 P. R. Spackman, M. J. Turner, J. J. McKinnon, S. K. Wolff, D. J. Grimwood, D. Jayatilaka and M. A. Spackman, CrystalExplorer: a program for Hirshfeld surface analysis, visualization and quantitative analysis of molecular crystals, *J. Appl. Crystallogr.*, 2021, **54**, 1006–1011.

48 J. J. Mckinnon, D. Jayatilaka and M. A. Spackman, Towards quantitative analysis of intermolecular interactions with Hirshfeld surfaces, *Chem. Commun.*, 2007, **3**, 3814–3816.

49 L. Speak, Structure validation in chemical crystallography, *Acta Crystallogr.*, 2009, **D65**, 148–155.

50 R. Černý and V. Favre-Nicolin, FOX: A Friendly Tool to solve nonmolecular structures from powder diffraction, *Powder Diffr.*, 2005, **20**, 359–365.

51 H. Elgahami, M. Ajili, T. Roisnel and A. Oueslati, Investigation of structural and ionic conductivity in the new organic-inorganic bromide: $[(C_3H_7)_4P]_2Cd_2Br_6$, *J. Solid State Chem.*, 2022, **311**, 123108.

52 N. Hannachi, K. Guidara, A. Bulou and F. Hlel, Structural characterization and AC conductivity of bis

tetrapropylammonium hexachlorado-dicadmate, $[N(C_3H_7)_4]_2Cd_2Cl6$, *Mater. Res. Bull.*, 2010, **45**, 1754–1761.

53 H. Elgahami, W. Trigui, A. Oueslati and F. Hlel, Structural, thermal analysis, and electrical conductivity of new organic-inorganic $[(C_4H_9)_4P]SbCl_4$ compound, *Ionics*, 2019, **25**, 1359–1371.

54 M. S. Lassoued, M. S. M Abdelbaky, A. Lassoued, S. Ammar, A. Gadri, A. Ben Salah and S. G. Granda, Structure characterization, photoluminescence and dielectric properties of a new hybrid compound containing chlorate anions of zincate (II), *J. Mol. Struct.*, 2018, **1158**, 221–228.

55 A. C. Dhieb, A. Valkonen, M. Rzaigui and W. Smirani, Synthesis, crystal structure, physico-chemical characterization and dielectric properties of a new hybrid material, 1-Ethylpiperazine-1,4-diium tetrachlorocadmate, *J. Mol. Struct.*, 2015, **1102**, 50–56.

56 P. M. Kumar, S. Badrinarayanan and M. Sastry, Nanocrystalline TiO_2 studied by optical, FTIR and X-ray photoelectron spectroscopy: correlation to presence of surface states, *Thin Solid Films*, 2000, **358**, 122–130.

57 D. Fredj, Ch. Ben Hassen, S. Elleuch, H. Feki, N. Ch. Boudjada, T. Mhiri and M. Boujelbene, Structural, vibrational and optical properties of a new organic–inorganic material: $(C_5H_8N_3)_2[BiCl_5]$, *Mater. Res. Bull.*, 2017, **85**, 23–29.

58 S. Sen, R. N. P. Choudhary and P. Pramanik, Structural and electrical properties of Ca2+ modified PZT electroceramics, *Phys. B*, 2007, **387**, 56–62.

59 A. Ingram, S. Wacke, Z. Czapla, C. Górecki and J. P. R. Szatanik, Structural phase transition in $[(C_2H_5)_4N][(CH_3)_4N]ZnCl_4$, *Phase Transitions*, 2019, **92**, 467–474.

60 M. Ben Gzaiel, K. Khirouni and M. Gargouri, Optical and electrical studies on the semi- conductor compound for the photovoltaic applications, *J. Organomet. Chem.*, 2021, **950**, 121992.

61 K. Karoui, A new hybrid layered perovskite $[CH_3–C_6H_4–NH_3]_2ZnBr_4$: Synthesis, crystal structure, optical and electrical properties, *J. Mol. Struct.*, 2020, **1203**, 127430.

62 A. K. Jonscher and M. S. Frost, Weakly frequency-dependent electrical conductivity in a chalcogenide glass, *Thin Solid Films*, 1976, **37**, 267–273.

63 T. Jadli, Y. Moualhi, A. Mleiki, H. Rahmouni, K. Khirouni and A. Cheikhrouhou, Electrical and dielectric properties of Sm0.55Sr0.45MnO3 compound, *J. Solid State Chem.*, 2021, **302**, 122378.

64 N. F. Mott, Conduction in glasses containing transition metal ions, *J. Non-Cryst. Solids*, 1968, **1**, 1–17.

65 M. A. Afifi, N. A. Hegab and A. E. Bekheat, Effect of annealing on the electrical properties of ln2Se3 thin films, *Vacuum*, 1995, **46**, 335–339.

66 G. A. Khan and C. A. Hogarth, The behaviour of SiOx/SnO thin dielectric films in an alternating electric field, *J. Mater. Sci.*, 1991, **26**, 17–20.

67 E. M. El-Menyawy, I. T. Zedan and H. H. Nawar, Electrical conductivity and dielectric relaxation of 2-(antipyrin-4-ylhydrazono)-2-(4-nitrophenyl) acetonitrile, *Phys. B*, 2014, **437**, 58–62.

68 S. Sahoo, U. Dash, S. K. S. Parashar and S. M. All, Frequency and temperature dependent electrical characteristics of $CaTiO_3$ nano-ceramic prepared by high-energy ball milling, *J. Adv. Ceram.*, 2013, **2**, 291–300.

69 S. Hajlaoui, I. Chaabane, A. Oueslati and K. Guidara, Anomalous dielectric behavior in centrosymmetric organic–inorganic hybrid bis-tetrapropylammonium hexachlorostannate. Crystal structure and properties, *Solid State Sci.*, 2013, **25**, 134–142.

70 A. Kyritsis, P. Pissis and J. Grammatikakis, Dielectric relaxation spectroscopy in poly (hydroxyethyl acrylates) water hydrogels, *J. Polym. Sci., Part B: Polym. Phys.*, 1995, **33**, 1737–1750.